NANO LETTERS

Letter

pubs.acs.org/NanoLett

Anisotropic Electron-Photon and Electron-Phonon Interactions in Black Phosphorus

Xi Ling,[*,†] Shengxi Huang,[†] Eddwi H. Hasdeo,[‡] Liangbo Liang,[§,⊥] William M. Parkin,[∥] Yuki Tatsumi,[‡] Ahmad R. T. Nugraha,[‡] Alexander A. Puretzky,[⊥] Paul Masih Das,[∥] Bobby G. Sumpter,[⊥,¶] David B. Geohegan,[⊥] Jing Kong,[†] Riichiro Saito,[‡] Marija Drndic,[∥] Vincent Meunier,[§] and Mildred S. Dresselhaus[*,†]

[†]Department of Electrical Engineering and Computer Science, Massachusetts Institute of Technology, Cambridge, Massachusetts 02139, United States

[‡]Department of Physics, Tohoku University, Sendai 980-8578, Japan

[§]Department of Physics, Applied Physics, and Astronomy, Rensselaer Polytechnic Institute, Troy, New York 12180, United States

[⊥]Center for Nanophase Materials Sciences and [¶]Computer Science and Mathematics Division, Oak Ridge National Laboratory, Oak Ridge, Tennessee 37831, United States

[∥]Department of Physics and Astronomy, University of Pennsylvania, Philadelphia, Pennsylvania 19104, United States

Supporting Information

ABSTRACT: Orthorhombic black phosphorus (BP) and other layered materials, such as gallium telluride (GaTe) and tin selenide (SnSe), stand out among two-dimensional (2D) materials owing to their anisotropic in-plane structure. This anisotropy adds a new dimension to the properties of 2D materials and stimulates the development of angle-resolved photonics and electronics. However, understanding the effect of anisotropy has remained unsatisfactory to date, as shown by a number of inconsistencies in the recent literature. We use angle-resolved absorption and Raman spectroscopies to investigate the role of anisotropy on the electron−photon and electron−phonon interactions in BP. We highlight, both experimentally and theoretically, a nontrivial dependence between anisotropy and flake thickness and photon and phonon energies. We show that once understood, the anisotropic optical absorption appears to be a reliable and simple way to identify the crystalline orientation of BP, which cannot be determined from Raman spectroscopy without the explicit consideration of excitation wavelength and flake thickness, as commonly used previously.

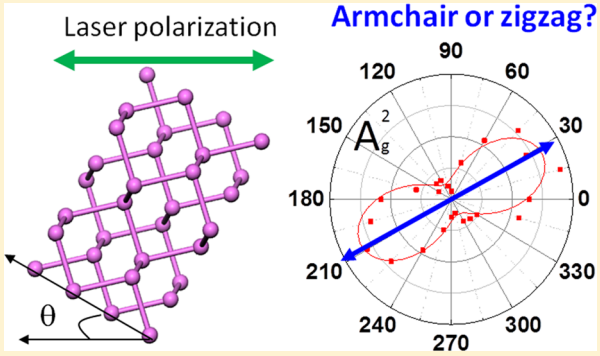

KEYWORDS: *In-plane anisotropy, Raman spectroscopy, optical absorption, crystalline orientation, optical selection rule*

In contrast to graphene[1] and some transition metal dichalcogenides,[2] numerous properties of black phosphorus (BP)[3] and other low-symmetry two-dimensional (2D) materials[4−6] show strong dependence on the in-plane crystalline orientation such as electrical mobility,[7] photoluminescence emission,[8] photoresponsivity,[9] and thermoelectric performance.[10] These properties are strongly associated with the behavior of electrons, phonons, and other quasiparticles, which can be probed by light−matter interaction using spectroscopy techniques including optical absorption and Raman scattering.[7,11−17] Here, we show, both experimentally and theoretically, how the electron−photon and electron−phonon interaction anisotropies in BP can be related to material thickness as well as photon and phonon energies.

The structure of a multilayer BP is shown in Figure 1, panel a. The *x*, *y*, *z* coordinates, adopted from the conventional notation for BP, are also labeled, where the *x*- and *z*- axes correspond to the armchair and zigzag directions of the BP layer plane, respectively.[18] High-resolution transmission electron microscopy (HRTEM) images and the diffraction patterns of selected areas are used to directly identify the armchair and zigzag directions. As shown in Figure 1, panel b, the atomically resolved HRTEM image indicates that the distance between every other phosphorus atom along the armchair (zigzag) direction is 0.45 nm (0.33 nm), consistent with the lattice parameters from our calculations and reported before.[13,16] To study the anisotropic electron−phonon and electron−photon interactions, polarized Raman spectra measurements and the corresponding TEM characterization were carried out on the same flake. The zigzag direction obtained from the TEM

Received: November 6, 2015
Revised: March 7, 2016
Published: March 10, 2016

DOI: 10.1021/acs.nanolett.5b04540
Nano Lett. 2016, 16, 2260−2267

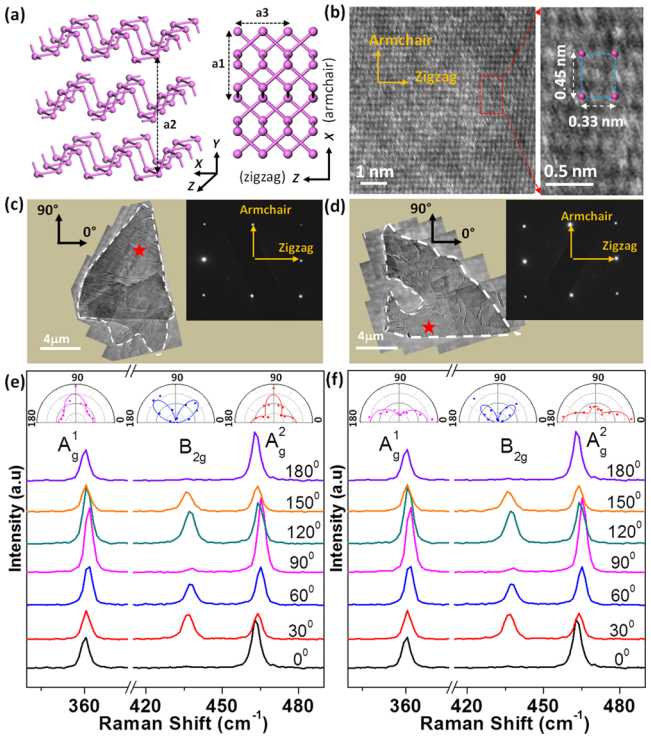

Figure 1. TEM characterization and anisotropic Raman scattering of BP. (a) Geometrical structure of multilayer black phosphorus. (b) Typical HRTEM image of BP. (c, d) TEM images of two BP flakes of different thickness and the corresponding diffraction patterns. The red stars label the position where the Raman spectra are collected. (e, f) The corresponding polarized Raman spectra of BP flakes in panels c and d, respectively. Here, 0° corresponds to the configuration with the incident laser polarization along the zigzag direction. Insets on top of panels e and f show the corresponding polar plots of the polarization dependent Raman intensity for the two BP flakes. The symbols are the experimental values, and the lines are least-squares fittings. The excitation wavelengths for panels e and f are both 633 nm (E_L = 1.96 eV).

characterization is defined as the 0° angle, from where we start to rotate the sample up to 180°. Raman spectra under different rotation angles were collected under the parallel configuration (i.e., the polarization of Raman scattered light parallel to that of the incident light), shown in Figure 1, panels e and f (633 nm laser excitation) and Supporting Information Figure S1 (532 nm laser excitation). Three typical Raman modes, A_g^1, B_{2g}, and A_g^2, are observed around 361, 438, and 466 cm^{-1}, respectively,[7,16] for both flakes with different thicknesses as identified from their optical contrast. The intensity of the A_g modes changes with the variation period of 180°, but the maximum intensity occurs at different polarization angles for the two flakes: either along armchair (the flake in Figure 1c) or zigzag direction (the flake in Figure 1d). These combined TEM/Raman measurements unambiguously prove that the maximum Raman intensity of A_g modes can switch direction from armchair to zigzag depending on flake thickness. Furthermore, B_{2g} behaves similarly for the two flakes, with an intensity variation period of 90° and minimum intensity corresponding to the armchair- and zigzag-polarized laser (insets in Figure 1e,f).

To understand the dependence of anisotropic Raman scattering on both the excitation wavelength and flake thickness, we studied 13 BP flakes with different thicknesses using three laser excitation wavelengths (532, 633, and 785 nm) (Supporting Information Section 2). The 13 BP flakes have the same crystalline orientation because they are mechanically exfoliated from the same bulk BP single crystal and are physically connected to each other (Supporting Information Figure S2). For all the 13 flakes under each wavelength, B_{2g} mode shows the same intensity anisotropy. However, the flakes differ regarding A_g^1 and A_g^2: the main axis (the direction for the maximum intensity) can be along either armchair or zigzag direction, strongly depending on the flake thickness and excitation wavelength.

According to the direction of the main axis of the polar plot, Table 1 shows polar plots of the Raman intensities of A_g modes for four typical flakes (a, b, c, and d) with thicknesses of around 5, 20, 40, and 200 nm, respectively. Here, 0° is an arbitrary angle corresponding to the sample configuration at the start of the rotation. First, we observed that with the same excitation wavelength, the direction of the main axis of the polar plot changes between armchair and zigzag when the flake thickness increases. Taking the 532 nm excitation data (E_L = 2.33 eV) as an example, for the 5 nm flake, both A_g^1 and A_g^2 show the maximum intensity at 30° and 210°. When the flake thickness increases to 20 and 40 nm, the polarization dependence of A_g^1 becomes very weak, while A_g^2 still shows a polarization dependence consistent with results found for the 5 nm flake. For the 20 nm flake, the polarization dependence shows remarkable secondary maxima for A_g^2 at 120° and 300°, which are due to the large phase difference between the complex Raman tensor elements *a* and *c* (discussed in detail later).[12] With the thickness of BP flakes increasing to 200 nm, the main axes of the polar plots for both A_g^1 and A_g^2 are at 120° and 300°, perpendicular to those for the 5 nm flake. We also observe a strong dependence of the main axis direction on the laser excitation wavelength. As shown in Table 1 and Supporting Information Table S1, for the same flake, the main axes of the polar plots for 532, 633, and 785 nm excitations (E_L = 2.33, 1.96, and 1.58 eV) can rotate by 90° and be along either 30° or 120°. These results conclusively demonstrate that the main axes of A_g modes can switch between armchair and zigzag directions depending on the flake thickness and excitation wavelength, which is of significance since it should settle the existing debate in the literature about whether the A_g main axis is along armchair or zigzag.[8,12,13,15] Our systematic study suggests that all of previous works[8,12,13,15] are correct but correspond to the presence of multiple independent variables such as different sample thicknesses and excitation wavelengths. Therefore, our results establish that caution is required when Raman spectroscopy is employed for BP crystalline orientation determination. An alternative approach (i.e., angle-resolved optical absorption technique) that is both reliable and simple will be discussed further.

The anisotropic interference effect could contribute to the thickness dependence of anisotropic Raman scattering but is not the only contributing factor as it cannot explain the excitation laser energy dependence.[17] To reveal the origin of the observed dependence of the anisotropy of the Raman scattering, we carried out in-depth analyses using density functional theory (DFT) and quantum perturbation theory. The Raman scattering process involves the electron−photon and electron−phonon interactions (Supporting Information Section 4).[19] The E_L-dependent Raman intensity for a ν phonon mode can be written as

DOI: 10.1021/acs.nanolett.5b04540
Nano Lett. 2016, 16, 2260−2267

Table 1. Four Typical Categories of the BP Flakes with the Anisotropic Raman Scattering under Different Incident Laser Wavelengths. The Blue and Green Arrows Indicate the Main Axes of the Polar Plots. The Data for the 5 nm Flake under 785 nm Laser Excitation Is Not Included in the Table Because of the Weak Raman Signal

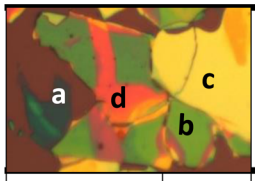		a (~5 nm)	b (~20 nm)	c (~40 nm)	d (~200 nm)
532 nm excitation	A_g^1	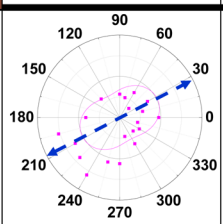	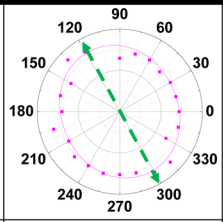	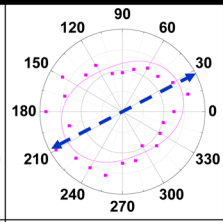	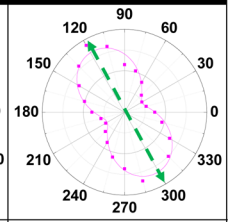
	A_g^2	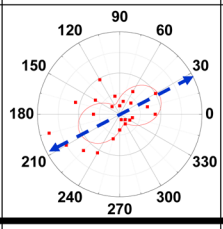	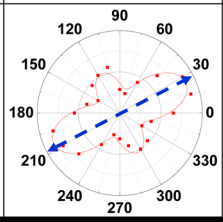	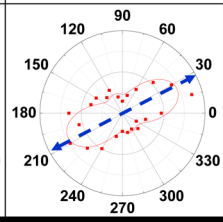	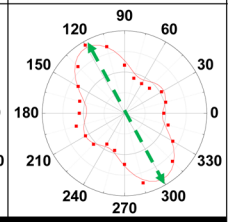
633 nm excitation	A_g^1	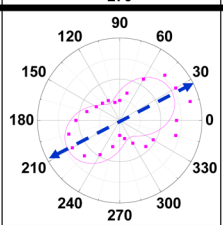	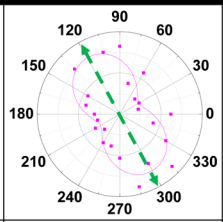	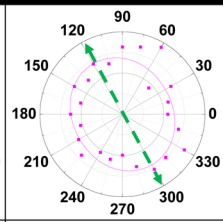	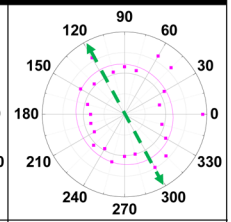
	A_g^2	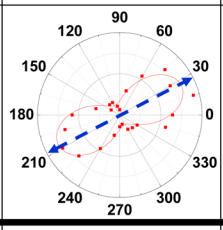	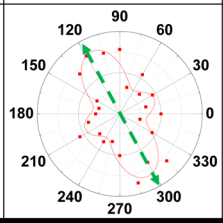	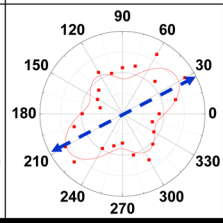	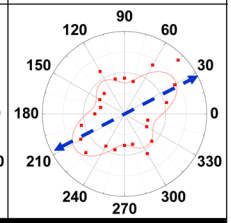
785 nm excitation	A_g^1	----	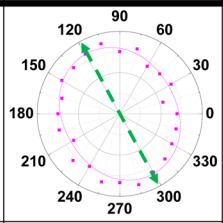	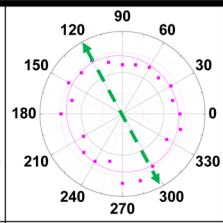	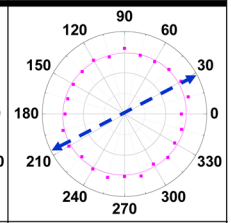
	A_g^2	----	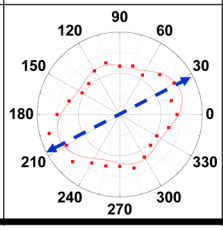	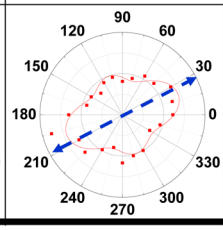	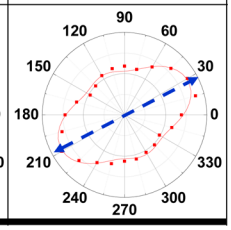

$$I_\nu(E_L) = \left| \sum_{i,m,m'} \frac{\langle f|H_{op}|m'\rangle\langle m'|H_{ep}^\nu|m\rangle\langle m|H_{op}|i\rangle}{(E_L - \Delta E_{mi})(E_L - \hbar\omega_\nu - \Delta E_{m'i})} \right|^2 \quad (1)$$

where $\langle f| = \langle i|$; E_L is the laser photon energy; $\Delta E_{mi} = E_m - E_i - i\gamma$; E_i, E_m, and $E_{m'}$ are the energy of the initial electronic state i and intermediate states m and m', respectively; and γ is the broadening factor. $\langle m|H_{op}|i\rangle$ and $\langle f|H_{op}|m'\rangle$ correspond to optical absorption and emission processes, which are related to the electron−photon interaction only, while $\langle m'|H_{ep}^\nu|m\rangle$ is the electron−phonon interaction. From Fermi's Golden Rule, the optical absorption coefficient α obeys:

$$\alpha(E_L) \propto \sum_{m,i} |\langle m|H_{op}|i\rangle|^2 \delta(E_m - E_i - E_L) \quad (2)$$

DOI: 10.1021/acs.nanolett.5b04540
Nano Lett. 2016, 16, 2260−2267

When the electron−photon interaction Hamiltonian H_{op} is treated within the dipole approximation, the electron−photon matrix element $\langle m|H_{op}|i\rangle$ responsible for an optical transition between states i and m is given by

$$\langle m|H_{op}|i\rangle \propto \mathbf{P}\cdot\mathbf{D}_{mi} \quad (3)$$

where $\mathbf{P}$ is the polarization vector of the incoming light, and the dipole vector $\mathbf{D}_{mi}$ is defined as $\boldsymbol{D}_{mi} = \langle m|\nabla|i\rangle$.[20] To obtain a nonvanishing $\langle m|H_{op}|i\rangle$, $\mathbf{D}_{mi}$ should have a nonzero component parallel to the light polarization vector $\mathbf{P}$. Therefore, the selection rule for the optical transition determines which two energy bands are involved in the electron transition for a given incident excitation energy with a specific light polarization (further details in Supporting Information Section 4), resulting in a different value of $\langle m|H_{op}|i\rangle$ and in turn different α for different incident light polarizations and different excitation photon energies.

Figure 2, panel a shows the calculated optical absorption coefficient α for monolayer, bilayer, trilayer, 10-layer, and bulk

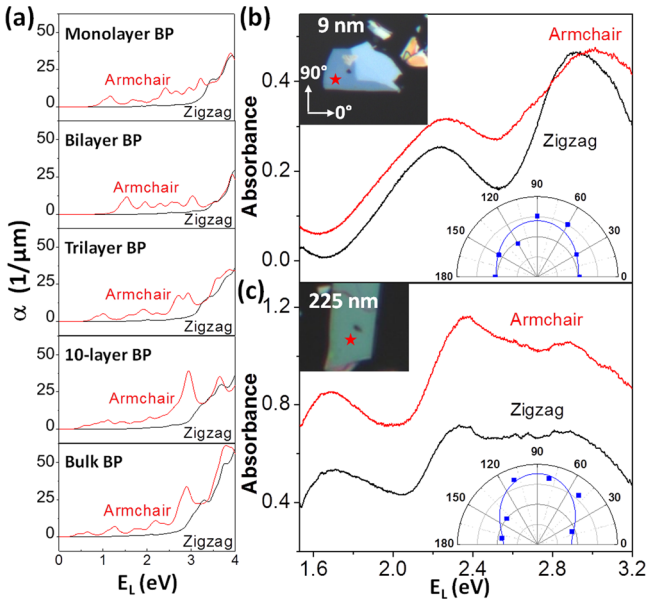

Figure 2. Anisotropic absorption of BP flakes with different thicknesses. (a) Calculated absorption coefficient α as a function of laser energy for monolayer, bilayer, trilayer, 10-layer, and bulk BP. (b, c) Typical absorbance spectra of (b) a thin and (c) a thick BP flake with incident light polarization along the armchair and zigzag directions. Insets: optical images and corresponding polar plots of the absorbance at 633 nm (E_L = 1.96 eV) versus the sample rotation angle in a plane normal to the flake. The symbols are the experimental values, and the lines are least-squares fittings. The red stars in the insets label the sample measurement positions. 0° and 90° corresponds to the zigzag and armchair directions, respectively.

BP under armchair- and zigzag-polarized light excitations. The calculated absorption of zigzag-polarized light (black line) starts from around 3.0 eV, while for armchair-polarized light (red line), the absorption starts at a much lower photon energy (i.e., starting at the optical gap). In addition, the calculations indicate that BP absorbs more visible light polarized along the armchair than along the zigzag direction. Moreover, from monolayer to bulk BP, the calculated α does not change significantly with the thickness for the same light polarization (Figure 2a), indicating that the absorbance ($A = \alpha l$) should increase with thickness (l).

We further measured the absorption spectra of the BP flakes with different thicknesses using a microabsorption setup. The unpolarized light absorbance A indeed increases with the BP thickness l (Supporting Information Figure S5). The absorbance changes when the incident light polarization is modified. Figure 2, panels b and c show the typical absorbance spectra with both armchair- and zigzag-polarized incident light for a thin (∼9 nm) and a thick (∼225 nm) flakes, and the corresponding polar plots of the absorbance at 1.96 eV versus the laser polarization are shown in the insets. Similar characteristics of anisotropic absorbance were observed at 2.33 and 1.58 eV (Supporting Information Figure S6). Note that we can directly identify armchair and zigzag directions of the BP crystals through the anisotropic optical absorption because as indicated by our calculations and previous works,[12,14,21] the absorption along the armchair direction should be larger than that along the zigzag one in the visible spectral range for all flake thicknesses due to the fact that the imaginary part of refractive index of BP (i.e., the extinction coefficient) in the armchair direction is notably larger than in the zigzag direction.[22] The simple anisotropic optical absorption involves only electron−photon interaction and hence provides a reliable alternative for crystalline orientation identification, while Raman scattering involves both electron−photon and electron−phonon interactions and thus is much more complicated. For example, A_g^2 Raman intensities of two flakes in Figure 2 exhibit opposite trend (Supporting Information Figure S7) due to the more complicated anisotropy of the electron−phonon interaction.

To analyze the anisotropy of electron−phonon interaction, first, the band structures of monolayer, bilayer, trilayer, and bulk BP, as well as the symmetry assignments for all bands at the Γ point, were calculated (Supporting Information Figure S3). For different BP thicknesses, the electron band structures, as well as the symmetry assignments for each band, are different. Figure 3, panel a shows the calculated band structure of a trilayer BP. In particular, four energy bands with

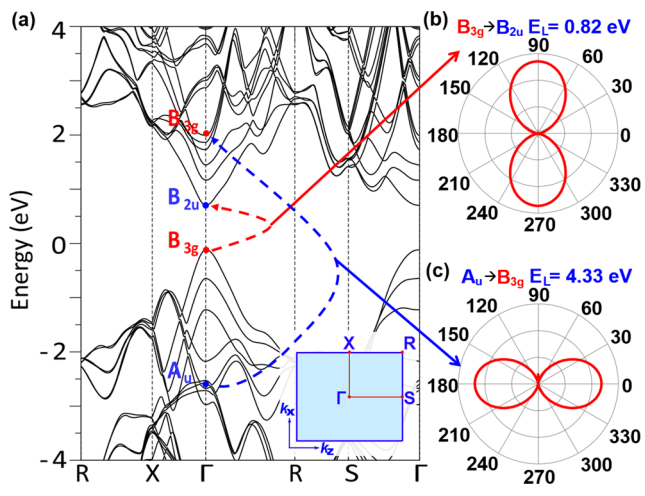

Figure 3. Optical selection rules in black phosphorus and the calculated anisotropic absorption. (a) Calculated electronic band structure $E(k)$ of trilayer BP. B_{3g} bands are indicated by red labels, while B_{2u} and A_u bands are indicated by blue labels at the Γ point. Inset: 2D Brillouin zone of trilayer BP. (b, c) Calculated polarization dependence of the optical transition probability (b) from B_{3g} to B_{2u} and (c) from A_u to B_{3g} as indicated in panel a. Here, 0° (90°) corresponds to the zigzag (armchair) direction of BP.

DOI: 10.1021/acs.nanolett.5b04540
Nano Lett. 2016, 16, 2260−2267

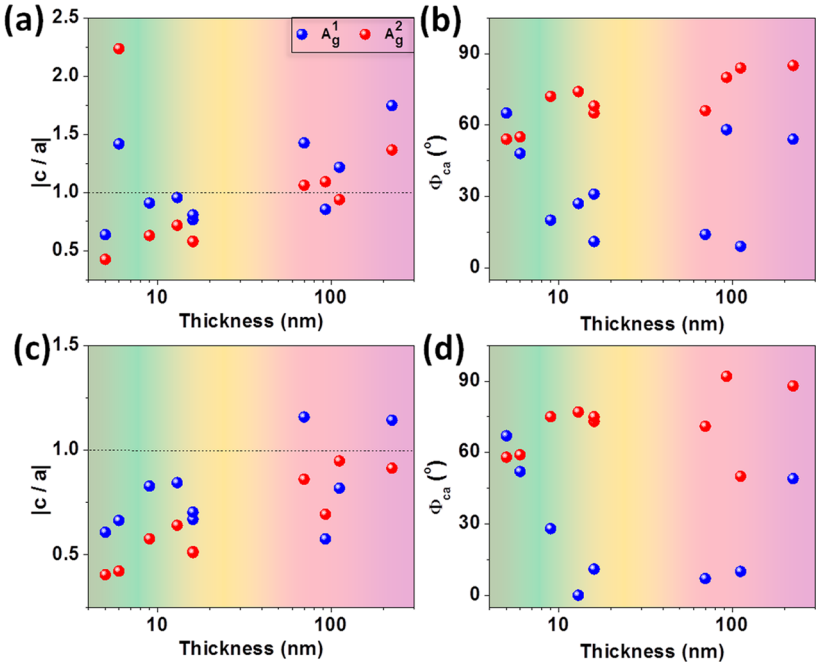

Figure 4. (a, c) $|c/a|$ and (b, d) Φ_{ca} as a function of the thickness of BP flakes. The data are from the anisotropic Raman spectra of BP with different thicknesses under 633 nm (E_L = 1.96 eV) laser excitation wavelength. (a, b) and (c, d) The results before and after the elimination of interference effect, respectively. Data in blue and red are for the A_g^1 and A_g^2 modes, respectively. The horizontal dashed line in panels a and c indicates $|c/a| = 1$. Panels a–d are divided horizontally with color shades corresponding to the thicknesses in Table 1: dark green, green, yellow, and pink correspond to thicknesses of approximately 5, 20, 40, and 200 nm, respectively.

symmetries B_{2u}, B_{3g}, and A_u are labeled. Figure 3, panels b and c show two typical examples of the optical absorption for trilayer BP with E_L = 0.82 eV and E_L = 4.33 eV, respectively. For E_L = 0.82 eV, the electron transition occurs between the energy bands $B_{3g} \rightarrow B_{2u}$. The anisotropic absorption for this case shows that the maximum (minimum) absorption occurs when the laser polarization is along armchair (zigzag) due to the symmetry, shown in Figure 3, panel b, while for E_L = 4.33 eV, the $A_u \rightarrow B_{3g}$ transition occurs with the reverse anisotropic absorption due to the different symmetry, shown in Figure 3, panel c. Other than the transitions shown in Figure 3, panels b and c, $B_{1u} \rightarrow A_g$ transition with E_L = 2.00 eV and $A_g \rightarrow B_{3u}$ transition with E_L = 5.86 eV contribute to the maximum absorption along armchair and zigzag directions, respectively (Supporting Information Figure S4), consistent with the results shown in Figure 2, panel a that the absorption along armchair is preferable over zigzag in the visible spectral range. In Raman scattering, H_{ep}^{ν} selects the symmetry of $|m\rangle$ and $|m'\rangle$, which should have the same and different symmetries for A_g and B_{2g} modes, respectively, and the shape of the polar plot of the Raman intensity should be the product of the two anisotropic electron–photon interaction processes if we assume that the electron–phonon interaction H_{ep}^{ν} has no polarization dependence (Supporting Information Section 4). Under this assumption, the anisotropic Raman intensities of A_g modes would always show a variation period of 180° with the main axis along armchair direction with laser excitation in the visible spectral range (i.e., the same as for the anisotropic absorption, Supporting Information Figure S4d). Obviously, this conflicts with our experimental observation that the anisotropy of A_g modes is more complicated than the anisotropy of optical absorption, and is intricately dependent on the thickness, excitation wavelength, and phonon energy. Therefore, our angle-resolved spectroscopy measurements successfully revealed the anisotropic electron–phonon interaction in BP.

Since electron–phonon interaction is a governing parameter for electrical, thermal, thermoelectric, and superconductive properties in materials,[1,23–25] our findings provide rich information for the study of anisotropic 2D materials. For instance, the weaker polarization dependence of A_g^1 compared to A_g^2 indicates that the out-of-plane vibrations (A_g^1) couple less anisotropically with in-plane electronic states compared to the in-plane vibrations (A_g^2).[23,25,26] In addition, the selectivity of the Raman anisotropy to the flake thickness and laser energy (Table 1 and Supporting Information Table S1) indicates that the electrons couple strongest to A_g phonons in either armchair or zigzag direction, depending on the symmetries of the involved electronic states (Figure 3a and Supporting Information Figure S3). Therefore, our combined angle-resolved Raman and optical absorption measurements facilitate the understanding of the electron–phonon interaction in anisotropic 2D materials.

The anisotropic Raman scattering can also be numerically understood from a semiclassical perspective. Since the Raman tensor is related to the derivative of the complex dielectric tensor with respect to the phonon vibration (the imaginary part of the dielectric tensor corresponds to optical absorption), the Raman tensor of an A_g mode, $\tilde{R}(A_g) = \begin{pmatrix} a & \cdot & \cdot \\ \cdot & b & \cdot \\ \cdot & \cdot & c \end{pmatrix}$, is complex (Supporting Information Section 8).[12] The corresponding Raman intensity under the parallel configuration is therefore

$$I_{A_g}^{\parallel} = |(\sin\theta, 0, \cos\theta)\tilde{R}(\sin\theta, 0, \cos\theta)^T|^2$$
$$= |a|^2\left[\left(\sin^2\theta + \left|\frac{c}{a}\right|\cos\Phi_{ca}\cos^2\theta\right)^2 + \left|\frac{c}{a}\right|^2\sin^2\Phi_{ca}\cos^4\theta\right] \quad (4)$$

DOI: 10.1021/acs.nanolett.5b04540
Nano Lett. 2016, 16, 2260–2267

where θ is the angle between the laser polarization and zigzag direction, and Φ_{ca} is the phase difference between the Raman tensor elements c and a. The amplitude ratio $|c/a|$ and Φ_{ca} are the indicators of the in-plane anisotropy in BP. From eq 4, $|c/a| > 1$ or $|c/a| < 1$ determines whether the main axis is along zigzag or armchair direction, and Φ_{ca} is positively correlated with the strength of the secondary maximum on the Raman polarization profile. The $|c/a|$ and Φ_{ca} values, obtained by directly fitting the experimental Raman polar plot with eq 4, are shown in Figure 4, panels a and b for both A_g^1 and A_g^2 with different thicknesses under 633 nm laser excitation. Note that optical interference has proved to considerably affect or enhance Raman intensities for layered materials such as multilayer graphene, MoS_2, etc.[27,28] Similar interference effect can also occur in BP.[17] More importantly, because of its unique in-plane anisotropy as discussed earlier (i.e., different refractive indices in the zigzag and armchair directions, and the imaginary part in particular), the interference enhancement effect is also polarization-dependent. To evaluate the importance of this effect, we calculated the interference enhancement factors of the A_g modes along the zigzag and armchair directions (more details about the calculations in Methods). For the three laser lines we used, the interference enhancement is stronger when the incident polarization is along the zigzag direction (Supporting Information Section 10) due to the weaker absorption in that direction. As shown in Figure S10 in the Supporting Information, the ratio of the enhancement factors between the zigzag and the armchair directions varies significantly with the BP thickness, which in turn can influence the thickness dependence of Raman intensity ratio $|c/a|$ between the zigzag and the armchair directions. In Figure 4, panels c and d, we eliminate the effect of interference on Raman intensity, and thus the $|c/a|$ and Φ_{ca} values shown are intrinsically from the BP flakes. While $|c/a|$ ratios do not show a clear evolution trend in Figure 4, panel a, the $|c/a|$ ratios in Figure 4, panel c show a roughly increasing trend with increasing thicknesses and are generally smaller than 1, in agreement with results from ref 17. This suggests that after elimination of interference effect, the maximum intensities of anisotropic Raman are generally along the armchair direction, thus the thickness dependence becomes simpler. By comparing Figure 4, panels b and d, we notice that Φ_{ca} also changes after the elimination of interference effect. These phenomena indicate that the interference effect is considerable for the complex thickness dependence of Raman polarization. However, it is not sufficient to explain all experimental observations. In fact, it is not reasonable that A_g^1 and A_g^2 modes can show different Raman anisotropy if interference effect was the dominating contributor. Moreover, $|c/a|$ ratios are still different from flakes with different thicknesses. These results can be attributed to the quantum effect of optical transition selection rule, as we have explained before. The combination of the quantum theory and interference effect can explain all the observations. Φ_{ca} is relatively small for A_g^1 compared to A_g^2 with different thicknesses, which is also reflected in Table 1 and Supporting Information Table S1 where the secondary maxima of A_g^1 are not obvious. As discussed earlier, this may be because the out-of-plane vibration A_g^1 is relatively insensitive to in-plane anisotropy. In contrast, Φ_{ca} is relatively large for A_g^2 because of its in-plane vibration.

In conclusion, we have uncovered the origins of the anisotropic light−matter interactions in BP including the electron−photon and electron−phonon interactions. The process and selection rule we revealed in BP is applicable to any other anisotropic materials such as gallium telluride (GaTe) and tin selenide (SnSe). Therefore, our work offers key insights into the light−matter interaction in anisotropic layered materials, thereby paving a coherent route for advancing the study of their anisotropic electrical, thermal, and thermoelectric properties.

Methods. *Sample Preparation and Characterization.* BP flakes were prepared on 300 nm SiO_2/Si or glass substrates by mechanical exfoliation from a bulk BP single crystal, and the flakes were immediately coated with a PMMA film (∼300 nm thick) to avoid degradation. The location of each flake was identified using an optical microscope. The thickness of each BP flake was measured by atomic force microscopy (AFM).

Raman Characterization. Raman spectra were collected on a Horiba Jobin-Yvon HR800 system equipped with three laser lines (532, 633, and 785 nm). A 100× objective was used to focus the laser beam on the sample. The spot size of the laser was approximately 1 μm. The laser power was about 1 mW for the 532 nm laser, 10 mW for the 633 nm laser, and 20 mW for the 785 nm laser. For the polarization-dependence measurements, the sample was mounted on a rotation stage, and the measurements were performed under the parallel configuration. The spectral parameters were obtained by fitting the peaks using Lorentzian/Gaussian mixed function.

Microabsorption Measurement. Exfoliated BP flakes were transferred on a quartz substrate for absorption measurements. The absorption spectra were measured using a home-built microabsorption setup based on a combination of inverted and upright microscopes that were used to focus the incident white light beam onto a BP flake and to collect the transmitted light. The white light was generated using a laser driven light source (EQ-99XFC, Energetiq) with fiber optic coupled output (25 μm diameter fiber). A reduced image of the output fiber face on the upper surface of the quartz substrate (spot size ∼1.5 μm) was formed using two microscope objectives (a 5×-collimating objective, NA (numeric aperture) = 0.1; and a 100×-long working distance objective, NA = 0.8 in the inverted microscope). The transmitted light was collected by a 50×-objective (NA = 0.5) in the upright microscope and analyzed by a spectrometer (Spectra Pro 2300i, f = 0.3 m) equipped with a CCD camera (Pixis 256BR, Princeton Instruments). Since the reflection shows weaker anisotropy compared to the absorption in BP,[9,29] we expect that the anisotropic feature of the measured optical spectra in Figure 2, panels b and c is mainly contributed by the anisotropic absorption of BP, and thus the contribution of reflection is neglected in our measurement. The absorbance (A) was calculated simply as $A = \ln(I_0/I)$ where I_0 and I are the light intensities transmitted through the quartz substrate nearby a BP flake location and through a BP flake, respectively. For polarized microabsorption measurements, the incident white light was linearly polarized using a Glan-Taylor polarizer.

TEM Characterization. To transfer the BP flakes onto the TEM grid, we sonicated the bulk BP in DMF solvent for 20 min. Then a C-flat TEM grid was immersed into the BP solution for 1 min. Finally, the TEM grids were removed from solution and dried in air. Aberration-corrected STEM images were obtained in a JEOL ARM 200CF operated at 80 keV. HRTEM images and selected-area diffraction images were taken in a JEOL 2100 operated at 200 keV. A 1 μm selected-area aperture was used; the diffraction images correspond to a roughly 1 μm diameter region of the samples.

DOI: 10.1021/acs.nanolett.5b04540
Nano Lett. 2016, 16, 2260−2267

DFT Calculations. Plane-wave DFT calculations were performed using the VASP package equipped with projector augmented wave (PAW) pseudopotentials for electron−ion interactions.[30] The exchange−correlation interactions were considered in the generalized gradient approximation (GGA) using Perdew−Burke−Ernzerhof (PBE) functional. The interlayer interactions were included using the van der Waals (vdW) density functional method optB88-vdW. For bulk BP, both atoms and cell volume were allowed to relax until the residual forces were below 0.001 eV/Å, with a cutoff energy set at 500 eV and a 9 × 4 × 12 k-point sampling in the Monkhorst−Pack scheme. By taking the in-plane armchair direction as the *x*-axis, the out-of-plane direction as the *y*-axis, and in-plane zigzag direction as the *z*-axis, the optimized lattice parameters in our DFT calculations for bulk BP are a_1 = 4.45 Å, a_2 = 10.67 Å, and a_3 = 3.35 Å. Monolayer, bilayer, trilayer, and 10-layer BP systems were then modeled by a periodic slab geometry using the optimized in-plane lattice constants of the bulk. A vacuum region of at least 18 Å in the out-of-plane direction was used to avoid spurious interactions with replicas. For the 2D slab calculations, all atoms were relaxed until the residual forces were below 0.001 eV/Å and 9 × 1 × 12 k-point samplings were used. As GGA−PBE *x*c functional tends to underestimate energy separations between valence and conduction bands, electronic bands were then updated by the hybrid functional (HSE06) method.[14] By extracting the important outputs from the DFT-HSE06 calculations including the electronic energy dispersion, electronic wave function coefficients, and symmetry information on the wave functions, we can determine whether an electronic transition is preferable to armchair-polarized or zigzag-polarized incident light based on eqs 2 and 3. It allows us to calculate the optical transition probability between two specific electronic states at a particular *k*-point via the electronic energy dispersions and wave function coefficients, while the symmetry information was used to analyze the selection rule for optical absorption and the phonon mode, as shown in Figure 3.

To compute the absorption coefficient $\alpha(E_L)$ considering the contributions from all electronic states across the Brillouin zone, the energy dependent complex dielectric function ϵ was then calculated by summation over all valence/conduction bands at every *k*-point in the Brillouin zone. The number of empty conduction bands was set to be triple that of occupied valence bands. By using the armchair-direction and zigzag-direction components of the dielectric function ϵ, we can compute the optical absorption coefficient $\alpha(E_L)$ along the armchair and zigzag directions (shown in Figure 2a), respectively, based on the formula[14] $\alpha(E_L) = \frac{E_L \mathrm{Im}(\epsilon)}{\hbar c n}$. E_L is the energy, $n = \sqrt{\frac{\sqrt{\mathrm{Re}(\epsilon)^2 + \mathrm{Im}(\epsilon)^2} + \mathrm{Re}(\epsilon)}{2}}$ is the real part of the complex refractive index, $\mathrm{Re}(\epsilon)$ and $\mathrm{Im}(\epsilon)$ are the real and imaginary parts of the dielectric function ϵ, $\hbar$ is the reduced Planck constant, and *c* is the speed of light. Such method yields consistent results with the approach discussed in eqs 2 and 3, particularly regarding the optical absorption anisotropy that the absorption along armchair direction is larger than that along zigzag direction in the visible spectral range.

For BP, the complex refractive index is expressed as $n^* = \sqrt{\epsilon} = n + ik$, where the real part *n* is the usual refractive index, and the imaginary part *k* is the extinction coefficient. On the basis of these quantities, we have absorption $\alpha = \frac{4\pi k}{\lambda}$ and reflection $R = \frac{(n-1)^2 + k^2}{(n+1)^2 + k^2}$ for the BP/air interface under normal incidence. According to our calculations and a previous experimental work,[26] *n* is notably larger than *κ*, and then $R \approx \frac{(n-1)^2}{(n+1)^2}$. Compared to *κ*, *n* shows much weaker dependence on the crystalline orientation. This leads to weaker anisotropy of reflection than that of the absorption in BP.

Enhancement Factor by Classical Interference Effect Calculation. When the thicknesses of BP flakes and the substrate are comparable with the wavelength of light, we expect a classical interference effect due to multiple reflections in BP/substrates layers as reported by refs 17 and 27. This interference effect depends on the polarization of light due to the different refractive indices in the armchair and zigzag direction of BP. The net enhancement of incident light F_{ex} caused by multiple reflections at a position *x* measured from the BP surface is given by[27]

$$F_{ex}(x) = t_{01}\frac{(1 + r_{12}r_{23}e^{-2i\beta_2^{ex}})e^{-i\beta_x^{ex}} + (r_{12} + r_{23}e^{-2i\beta_2^{ex}})e^{-i(2\beta_1^{ex} - \beta_x^{ex})}}{1 + r_{12}r_{23}e^{-2i\beta_2^{ex}} + (r_{12} + r_{23}e^{-2i\beta_2^{ex}})r_{01}e^{-2i\beta_1^{ex}}}$$

where $t_{ij} = 2n_i/(n_i + n_j)$ and $r_{ij} = (n_i - n_j)/(n_i + n_j)$ are the Fresnel transmittance and reflectance coefficients, respectively, at the interfaces of the *i*th and *j*th layer with *i,j* indices given by air (0), BP (1), 0.5 mm thick quartz (2), and air (3). n_i is the complex refractive index of the *I*th layer. $\beta_x^{ex} = 2\pi x n_1/\lambda_{ex}$ and $\beta_i^{ex} = 2\pi d_i n_i/\lambda_{ex}$ are the phase factors with d_i the thickness of the *I*th layer and λ_{ex} the excitation wavelength.

The net enhancement of scattered light $F_{sc}(x)$ due to multiple reflections at a position *x* measured from the BP surface is given by

$$F_{sc}(x) = t_{10}\frac{(1 + r_{12}r_{23}e^{-2i\beta_2^{sc}})e^{-i\beta_x^{sc}} + (r_{12} + r_{23}e^{-2i\beta_2^{sc}})e^{-i(2\beta_1^{sc} - \beta_x^{sc})}}{1 + r_{12}r_{23}e^{-2i\beta_2^{sc}} + (r_{12} + r_{23}e^{-2i\beta_2^{sc}})r_{01}e^{-2i\beta_1^{sc}}}$$

where $\beta_x^{sc} = 2\pi x n_1/\lambda_{sc}$ and $\beta_i^{sc} = 2\pi d_i n_i/\lambda_{sc}$ are the phase factors for scattered light with a wavelength λ_{sc} related to the Raman shift of a particular spectrum. The total enhancement factors are then given by

$$F = N\int_0^{d_1} |F_{ex}(x)F_{sc}(x)|^2 \, dx$$

where *N* is the normalization constant. The observed Raman intensity is $R = I \times F$, where *I* is the intrinsic Raman intensity considering only electron−photon and electron−phonon interactions. We use the refractive indices for armchair and zigzag BP from ref 17.

■ ASSOCIATED CONTENT

Supporting Information

The Supporting Information is available free of charge on the ACS Publications website at DOI: 10.1021/acs.nanolett.5b04540.

Polarized Raman scattering intensities of the flakes in Figure 1 under 532 nm laser excitation; polar plots of the Raman intensities versus the sample rotation angle for 13 BP flakes; energy band structures and band symmetry of BP with different thicknesses; analysis of the anisotropic absorption and Raman scattering using the selection rules of the optical transition; thickness dependence of absorbance of BP; polarized absorbance at 2.33 and 1.58 eV of BP flakes in Figure 2; polarized Raman scattering

DOI: 10.1021/acs.nanolett.5b04540
Nano Lett. 2016, 16, 2260−2267

intensities of A_g^2 mode for the two typical flakes in Figure 2; semiclassical model of polarized Raman scattering; calculated anisotropic reflection and absorption of monolayer and bulk BP; calculated zigzag/armchair ratio of interference enhancement factor as a function of the sample thickness (PDF)

AUTHOR INFORMATION

Corresponding Authors

*Phone: +1-617-253-6864. E-mail: millie@mgm.mit.edu.
*Phone: +1-617-253-6860. E-mail: xiling@mit.edu.

Author Contributions

X.L. and S.H. contributed equally to this work. X.L., S.H., L.L., V.M., J.K., and M.S.D. initiated the project and designed the experiments. X.L., S.H., and A.A.P. performed experimental measurements and analyzed the data. W.P., P.D., and M.D. helped with the TEM characterization. E.H.H., Y.T., A.R.T.N., R.S., L.L., and V.M. performed the theoretical analysis. All authors discussed the results and contribute to the writing and revision of the manuscript.

Notes

The authors declare no competing financial interest.

ACKNOWLEDGMENTS

The authors acknowledge Professor Marcos A. Pimenta from Federal University of Minas Gerais in Brazil for helpful discussion. X.L., S.H., and M.S.D. at MIT acknowledge National Science Foundation grant 2DARE (EFRI-1542815) and U.S. Department of Energy Grant No. DE-SC0001299 for financial support. A.R.T.N. acknowledges the Leading Graduate Schools Program from Tohoku University for financial support. R.S. acknowledges MEXT Grant No. 25107005. V.M. acknowledges the support by NSF and the Office of Naval Research. L.L. was supported as a Eugene P. Wigner Fellow at the Oak Ridge National Laboratory. Microabsorption measurements were conducted at the Center for Nanophase Materials Sciences, which is sponsored at Oak Ridge National Laboratory by the Scientific User Facilities Division, Office of Basic Energy Sciences, U.S. Department of Energy. W.M.P., P.M.D., and M.D. acknowledge the NSF-MRSEC electron microscopy facility at the University of Pennsylvania and Dr. Robert Keyse for the use of the AC-TEM facility at Lehigh University. During the preparation of this manuscript, the authors became aware of a similar work published.[17]

REFERENCES

(1) Geim, A. K.; Novoselov, K. S. *Nat. Mater.* **2007**, *6* (3), 183−191.
(2) Wang, Q. H.; Kalantar-Zadeh, K.; Kis, A.; Coleman, J. N.; Strano, M. S. *Nat. Nanotechnol.* **2012**, *7* (11), 699−712.
(3) Ling, X.; Wang, H.; Huang, S.; Xia, F.; Dresselhaus, M. S. *Proc. Natl. Acad. Sci. U. S. A.* **2015**, *112* (15), 4523−4530.
(4) Liu, F.; Shimotani, H.; Shang, H.; Kanagasekaran, T.; Zólyomi, V.; Drummond, N.; Fal'ko, V. I.; Tanigaki, K. *ACS Nano* **2014**, *8* (1), 752−760.
(5) Liu, E.; Fu, Y.; Wang, Y.; Feng, Y.; Liu, H.; Wan, X.; Zhou, W.; Wang, B.; Shao, L.; Ho, C.-H.; Huang, Y.-S.; Cao, Z.; Wang, L.; Li, A.; Zeng, J.; Song, F.; Wang, X.; Shi, Y.; Yuan, H.; Hwang, H. Y.; Cui, Y.; Miao, F.; Xing, D. *Nat. Commun.* **2015**, *6*, 6991.
(6) Zhao, L.-D.; Lo, S.-H.; Zhang, Y.; Sun, H.; Tan, G.; Uher, C.; Wolverton, C.; Dravid, V. P.; Kanatzidis, M. G. *Nature* **2014**, *508* (7496), 373−377.
(7) Xia, F.; Wang, H.; Jia, Y. *Nat. Commun.* **2014**, *5*, 4458.
(8) Wang, X.; Jones, A. M.; Seyler, K. L.; Tran, V.; Jia, Y.; Zhao, H.; Wang, H.; Yang, L.; Xu, X.; Xia, F. *Nat. Nanotechnol.* **2015**, *10* (6), 517−521.
(9) Yuan, H.; Liu, X.; Afshinmanesh, F.; Li, W.; Xu, G.; Sun, J.; Lian, B.; Curto, A. G.; Ye, G.; Hikita, Y.; Shen, Z.; Zhang, S.-C.; Chen, X.; Brongersma, M.; Hwang, H. Y.; Cui, Y. *Nat. Nanotechnol.* **2015**, *10* (8), 707−713.
(10) Fei, R.; Faghaninia, A.; Soklaski, R.; Yan, J.-A.; Lo, C.; Yang, L. *Nano Lett.* **2014**, *14* (11), 6393−6399.
(11) Ikezawa, M.; Kondo, Y.; Shirotani, I. *J. Phys. Soc. Jpn.* **1983**, *52* (5), 1518−1520.
(12) Ribeiro, H. B.; Pimenta, M. A.; de Matos, C. J. S.; Moreira, R. L.; Rodin, A. S.; Zapata, J. D.; de Souza, E. A. T.; Castro Neto, A. H. *ACS Nano* **2015**, *9* (4), 4270−4276.
(13) Lu, W.; Ma, X.; Fei, Z.; Zhou, J.; Zhang, Z.; Jin, C.; Zhang, Z. *Appl. Phys. Lett.* **2015**, *107* (2), 021906.
(14) Qiao, J.; Kong, X.; Hu, Z.-X.; Yang, F.; Ji, W. *Nat. Commun.* **2014**, *5*, 4475.
(15) Wu, J.; Mao, N.; Xie, L.; Xu, H.; Zhang, J. *Angew. Chem.* **2015**, *127* (8), 2396−2399.
(16) Sugai, S.; Shirotani, I. *Solid State Commun.* **1985**, *53* (9), 753−755.
(17) Kim, J.; Lee, J.-U.; Lee, J.; Park, H. J.; Lee, Z.; Lee, C.; Cheong, H. *Nanoscale* **2015**, *7* (44), 18708−18715.
(18) We found that in the literature, different coordinate notations have been used. For example, some use x as armchair, y as zigzag, z as out-of-plane directions, such as refs 7, 9, and 21; some use x as armchair, z as zigzag, y as out-of-plane (ref 12); some use z as armchair, x as zigzag, y as out-of-plane (ref 16). It should be mentioned that different notations render different notations of Raman modes. For example, if we use z as out-of-plane direction, the Raman modes are A_g^1, A_g^2, and B_{1g}, but if we use y as out-of-plane mode, the Raman modes are A_g^1, A_g^2, and B_{2g}. To keep the Raman modes symmetry notations consistent with most literature (A_g^1, A_g^2, and B_{2g}), we follow the notation from ref 12 and use x as armchair, z as zigzag, and y as out-of-plane direction.
(19) Jorio, A. *Raman Spectroscopy in Graphene Related Systems*; Wiley-VCH: Weinheim, Germany, 2011.
(20) Sakurai, J. J.; Napolitano, J. *Modern Quantum Mechanics*, 2nd ed.; Addison-Wesley: Boston, MA, 2011.
(21) Tran, V.; Soklaski, R.; Liang, Y.; Yang, L. *Phys. Rev. B: Condens. Matter Mater. Phys.* **2014**, *89* (23), 235319.
(22) Asahina, H.; Morita, A. *J. Phys. C: Solid State Phys.* **1984**, *17* (11), 1839−1852.
(23) Liao, B.; Zhou, J.; Qiu, B.; Dresselhaus, M. S.; Chen, G. *Phys. Rev. B: Condens. Matter Mater. Phys.* **2015**, *91* (23), 235419.
(24) Zhang, A.-M.; Zhang, Q.-M. *Chin. Phys. B* **2013**, *22* (8), 087103.
(25) Ma, Y.; Tse, J. S.; Klug, D. D.; Ahuja, R. *Phys. Rev. B: Condens. Matter Mater. Phys.* **2004**, *70* (21), 214107.
(26) Ling, X.; Liang, L.; Huang, S.; Puretzky, A. A.; Geohegan, D. B.; Sumpter, B. G.; Kong, J.; Meunier, V.; Dresselhaus, M. S. *Nano Lett.* **2015**, *15* (6), 4080−4088.
(27) Yoon, D.; Moon, H.; Son, Y.-W.; Choi, J. S.; Park, B. H.; Cha, Y. H.; Kim, Y. D.; Cheong, H. *Phys. Rev. B: Condens. Matter Mater. Phys.* **2009**, *80* (12), 125422.
(28) Gao, L.; Ren, W.; Liu, B.; Saito, R.; Wu, Z.-S.; Li, S.; Jiang, C.; Li, F.; Cheng, H.-M. *ACS Nano* **2009**, *3* (4), 933−939.
(29) Mao, N.; Tang, J.; Xie, L.; Wu, J.; Han, B.; Lin, J.; Deng, S.; Ji, W.; Xu, H.; Liu, K.; Tong, L.; Zhang, J. *J. Am. Chem. Soc.* **2016**, *138* (1), 300−305.
(30) Kresse, G.; Furthmüller, J. *Comput. Mater. Sci.* **1996**, *6* (1), 15−50.

DOI: 10.1021/acs.nanolett.5b04540
Nano Lett. 2016, 16, 2260−2267